Figure S1. Characterization and quantification of RGD behavior. Related to Figure 1.

A) Exemplar video frames (front view) showing hand locations in a representative reach to P4 at different time points during the reach.
B) Schematic of the measurement of hand rotation direction (black vector) and finger pointing direction (orange vector) as represented by key points on left digits. Hand postures at lift, advance endpoint and supinate for licking are shown.
C) Quantification of waterspout aiming score ($\cos(\delta)$).
D) Quantification of digit open size, quantified as the length of hand rotation vector.
E) Schematic for quantifying the hand rotation score ($\cos(\theta)$) relative to the horizontal vector (y). Besides wrist rotation movement, the hand rotation score is also a reflection of the palm-facing direction. Value 1 means the palm is facing upward and -1 indicates the palm facing downward. 0 means left hand is facing the right side, which is often the case at the reach endpoint for grasping.
F) Schematic for quantifying hand to mouth distance (d) and hand supination vector (s) upon lick. Hand was maintained close to the mouth and supinated during tongue protrusions.
G) Measurement of mouth opening size (black triangle).
H) Probability distribution of the temporal order of forelimb, hand, and oral movements. Results of 3924 trials from 99 sessions in 33 mice reaching for P2.
I) Exemplar movement variables at waterspout positions P1, P3 and P5.
J) –(O) Target position modulation of lift latency relative to water delivery (J), grasp probability after lift (K), path length (L), target aiming score difference between aim onset and aim end (M), probability of significant acceleration peaks during aim and advance (N), premature lick before waterspout contact (O). 70 sessions from 25 mice.

Figure S2. PN type-based cortex-wide calcium activity during RGD. Related to Figure 2.

A) Neocortical areas superimposed on a brain image registered to Allen CCF. MOB, main olfactory bulb; MOs, secondary motor cortex; MOp, primary motor cortex; RSP, retrosplenial cortex; SSp, primary somatosensory cortex; tr, trunk; ll, lower limb; ul/un, upper limb and unknown region; orf, orofacial; bfd, barrel field; VIS, visual cortex. White dots outline the cortex; yellow horizontal line shows olfactory bulb and neocortex boundary; yellow vertical line shows the midsagittal suture. See Methods.
B) Coronal brain sections showing the laminar pattern of PN types labeled by driver lines crossed to reporter mice, for neuronal types see Figure 2B.
C) Simultaneous immunostaining of Cux1 (red) and Tle4 (blue), with mRNA in situ hybridization of *Fezf2* (magenta) in *PlxnD1;Ai148* (green) mice, showing the spatial distribution patterns of PN types. Scale bar, 100 μm.
D) RGD behavior characterization after training at location P2. Top, lift and first hand-lick probability (Prob.) distribution relative to waterspout contact. 3651 trials in 99 sessions from 33 mice. Bottom, average lick frequency aligned to waterspout contact.
E) Average sequential activity frames with 200 msec interval centered on waterspout contact (black box) during RGD from P2. Average of 9 sessions from 5 mice for PN^{Emx1}; 7 sessions from 4

mice for IT^{Cux1}; 11 sessions from 4 mice for IT^{PlxnD1}; 12 sessions from 6 mice for PT^{Fezf2}; 10 sessions from 5 mice for CT^{Tle4}.

F) Average temporal calcium activity traces aligned to waterspout contact (vertical gray dash line) for different areas and PN populations when RGD from P2. Error shading: SEM.

Figure S3. Target modulation of cortical network activity during RGD. Related to Figure 2.

A) Details of the generalized linear encoding model (GLM). Original calcium dynamics (***Y***) is decomposed into a "spatial" factor ***U*** and a "temporal" factor ***V*** using singular value decomposition (SVD). 10 behavior variables were constructed as ***X*** regressors to predict the temporal components ***V*** with a GLM (***V*** ~ ***BX***). Ridge regularization and cross-validation were used to avoid overfitting. See Methods.

B) Summary and comparison of regions of interest (ROIs) from different neuron types. Top, ROIs by thresholding of normalized GLM performance from Figure 2F. Colors correspond to different PN types. Bottom, ROIs by thresholding of normalized activity from Figure 2E from 5 different waterspout locations.

C) Quantification of the performance of the GLM encoding model for different ROIs. Different colors correspond to different neuron populations.

D) Box plot of target location decoding accuracy of PN type (colored) activities in different ROIs in ipsilateral and contralateral cortex.

E) Comparison of average calcium activity between waterspout location P5 (color traces) and location P1 (gray traces) of ROIs. Arrows indicate increased ipsilateral activities across ROIs and PN types when reaching for P5 over P1. Shaded areas indicate SEM.

Figure S4. Photoinhibition screening across activity nodes and direct inhibition of PNs in MOs-c during RGD. Related to Figure 3.

A) ChR2-assisted closed-loop photoinhibition of cortical areas during RGD. Crosses ('x') represent the center of cortical regions as obtained in previous publications. From anterior to posterior: anterior lateral motor cortex (ALM; Guo, 2014), rostral forelimb area (RFA; Tennant, 2011), rostal forelimb orofacial area (RFO; An, 2023) and caudal forelimb area (CFA; Tennant, 2011) overlaps with primary motor cortex for the upper limb (Sauerbrei, 2020; Muñoz-Castañeda, 2022). Black squares indicate the center of region of interest. +, bregma; scale, 0.5 mm.

B) Distribution of supination latency relative to hand lift in closed-loop inhibition and control trials of each node in contralateral and ipsilateral hemisphere. All trials from 5 *Pvalb-ires-Cre;Ai32* mice were pooled. Two-sample Kolmogorov-Smirnov test.

C) Perturbation of RGD with MOs-c photoinhibition. A control trial is shown along with an inhibition trial as light was triggered during the advance phase. In the inhibition trial, advance was aborted, and the hand returned to the start position (turquoise trajectory), following which another failed attempt occurred. Constituent movements are color coded.

D) Closed-loop inhibition of cMOs-c (contralateral MOs-c) impaired movement progression represented as ethogram from an example session. Actions are color coded. The relative onset and duration of inhibition light for each trial are indicated with light cyan shades. Note inhibition attenuates the completion of the RGD movement.

E) Impairment of movement profiles with closed-loop MOs-c inhibition. Exemplar hand movements in relation to target, hand rotation, and licks from several consecutive control (gray) and inhibition (tortoise) trials are shown. Movement profiles are normalized. Note that upon termination of inhibition, animals immediately resumed and completed the action sequence of RGD.

F) Closed-loop cMOs-c inhibition resulted in increased hand reversals during reaches, decreased target contact after lift, supination after grasp, and hand lick after grasp. Data from 5 mice with 2-sample Kolmogorov-Smirnov test.
G) Viral expression of the inhibitory opsin GtACR1 in MOs-c of an *Emx1-Cre* mouse. Scale, 1 mm.
H) Attenuation of aim and grasp after lift, and supinate and lick after grasp upon closed-loop inhibition of cMOs-c PNs. Trials pooled from 5 PN^{Emx1} mice.
I) Slight decrease of lift probability during reaching for contralateral targets upon prolonged cMOs-c PN inhibition. A total of 14 sessions from 7 PN^{Emx1} mice. Same mice for all following panels. ANOVA, inhibition statistic $F_{1,56} = 10.74$, $p < 0.01$; inhibition × target $F_{4,56} = 4.46$, $p < 0.01$.
J) No significant effects on RGD actions when inhibiting iMOs-c (ipsilateral MOs-c) PN versus control; from 4 PN^{Emx1} mice. Wilcoxon rank sum test for digit opens size; ANOVA for others.

Error bars: SEM. *, p < 0.05; **, p < 0.01; ***, p < 0.001; n.s., not significant.

Figure S5. Dynamic activity tuning to RGD action phase and target location in MOs-c neurons. Related to Figure 4.

A) Raw activity traces of simultaneously recorded neurons using a linear silicon probe from an exemplar trial. Note the different spike patterns at different cortical depths.
B) Examples activity patterns of three simultaneously recorded neurons shown by peri-event histograms and raster plots aligned to the advance endpoint. Trials are sorted by the duration between hand lift (orange dots) and advance endpoint (purple solid line). Black ticks: first hand lick of each trial.
C) Neuronal activity at different neocortical depths relative to hand lift (0) from an example recording session.
D) Fraction of 921 activated neurons that peaked at different action phases during RGD. Note that more neurons showed peak activity during reach, grasp, and withdraw than during drink.
E) Spiking activity aligned to advance endpoint for all recorded neurons sorted by peak activity latency. Each row represents one individual neuron activity across five waterspout locations. A total of 1655 neurons from 111 sessions, of which 921 neurons were activated, 269 neurons were not significantly modulated, and 465 neurons were inhibited. Vertical dash lines represent advance endpoint (time 0).
F) Increase of movement encoding as the depth of recorded neurons increases. $R^2 = 0.125$, $p = 1.05e\text{-}41$. Movement encoding of individual neurons was represented by the deviance explained by a Poisson-GLM. See Methods.
G) Increase of peak activity as the depth of recorded neurons increases. $R^2 = 0.0653$, $p = 3.40e\text{-}15$.
H) Target modulation index negatively correlates with cortical depth. $R^2 = 0.0822$, $p = 6.97e\text{-}19$.
I) Transition probability of neuron activation state across action phases from reach to grasp-withdraw during RGD. Note the higher probability in maintaining either increased or decreased spiking across the two action phases.
J) Computational clustering of all activated neurons using non-negative matrix factorization across a range of cluster numbers. Cluster stability is represented with bootstrapped adjusted rand index (ARI). 5 clusters show the highest cluster stability. See Methods.
K) Sorted membership consensus matrix shows a strong within-cluster consensus and between-cluster antagonism.
L) Tight correlation between exemplar raw behavior profiles (gray) and GLM-predicted traces (orange) using simultaneously recorded spiking activity from an exemplar recording session. Behavior profiles include forward, upward, lateral hand position, and hand position in relation to waterspout or mouth. Spikes were binned in 20 msec bins to predict movement kinematics using GLM.

M) Performance of GLM in predicting hand-target distance is dependent on the number of simultaneously recorded units. y = 0.1861+0.0051x, R^2 = 0.262, p = 3.75e-8.

Figure S6. Optical tagging of PNs. Related to Figure 5.

A) Peri-event activity (top) and raster (bottom) representation of spiking activity of an optically tagged exemplar neuron aligned to blue light pulse onset. Inset shows the average waveform of light-evoked (blue) and regular spontaneous (gray) spikes. Vertical dashed line indicates blue light pulse (blue bar on top) onset. Note there are fast (within 10 msec) and delayed (between 20-40 msec) activations of spiking.

B) Light-evoked spike reliability, jitter, and latency of all neurons (gray and blue circles). Blue circles indicate optogenetically tagged neurons with high reliability, low light evoked spiking latency, and low latency jitter.

C) Light-evoked spiking activity of all identified neurons, including 22 IT^{Cux1}, 17 IT^{PlxnD1}, 63 PT^{Fezf2}, and 30 CT^{Tle4} neurons, arranged from top to bottom. Each row of the heatmap represents the z-score normalized activity of a neuron. Vertical dashed line indicates light pulse (blue bar) onset.

D) Average light-evoked activity of all tagged neurons across different neuron types. Right panel is a zoomed-in view of the gray area in the left panel, which indicates the delayed modulation upon brief light pulses. Horizontal dashed lines: 0 z-score.

E) Boxplots of recording depth, jitter and latency of light-evoked spike, and baseline firing rate of different PN types. Median ± interquartile range. Horizontal lines in boxplots indicate 75%, 50%, and 25% percentile. Whiskers represent data point span to 90% or 10% percentile.

Figure S7. PN-type specific behavioral correlates and properties of population dynamics. Related to Figure 5.

A) Hand movement trajectory with neural activity (colormap) superimposed from exemplar neurons of four different PN types. X, forward; Y, lateral; Z, upward positions. Scale, 5 mm.

B) Peri-event histogram and raster plot from optically tagged IT^{Cux1}, IT^{PlxnD1}, PT^{Fezf2} and CT^{Tle4} exemplar neurons. Spikes are aligned to advance endpoint (purple vertical line). Trials are sorted by the onset of hand lift (orange ticks). Vertical dashed line: advance endpoint.

C) Average firing rate of the four PN types at different RGD action phases.

D) Distribution of movement encoding performance of individual neurons. Movement encoding performance of individual neurons was represented by the deviance explained by a Poisson-GLM. PT^{Fezf2} and CT^{Tle4} comprise a higher fraction of neurons that reliably and robustly encode movement.

E) Target modulation index of distinct PN types across different action phases.

F) Cumulative proportion of variance explained after PCA decomposition of different PNs. Bootstrapped component number to explain 80% of the variance of 16 neurons for each neuron type: 4 for IT^{Cux1}, 3 for IT^{PlxnD1}, 3 for PT^{Fezf2} and 2 for CT^{Tle4} as indicated by the dashed line.

G) Smoothness of the population neural trajectory. Note the higher smoothness (lower jerkiness) in PT^{Fezf2} and CT^{Tle4} populations. Equal numbers of neurons (16 from each neuron type) were randomly selected for the analysis to eliminate the impact of neural number. The following metrics of population neural trajectory were all bootstrapped for comparison among neuron types.

H) Response distance between pairs of neural trajectories at advance endpoint for different PN types. Heatmap represents bootstrapped average Euclidean distance. Note overall larger response distance in IT^{Cux1} and the overall smaller response distance in CT^{Tle4}. Also note lower response distance between closer waterspout locations.

I) Dissimilarity in geometric shape of different pairs of population neural trajectories of different neuron types. Note overall lower shape similarity (higher dissimilarity) in IT^{Cux1} and the overall higher shape similarity (lower dissimilarity) in CT^{Tle4}.

Figure S8. MOs-c PN-type specific contribution to RGD. Related to Figure 6.

A) Cortical, striatal, and thalamic projections from different MOs-c PN types. IT neurons show projection to contralateral cortex and no projection to thalamus. Note the rare projection of IT^{Cux1} to striatum as compared with that of IT^{PlxnD1}. PT^{Fezf2} and CT^{Tle4} both project to thalamus, with CT^{Tle4} projections restricted only to thalamus. Scale, 1 mm.

B) Heatmap summary of the change of RGD constituent action occurrence-probability upon closed-loop inhibition of different PN types in MOs-c.

C) Reduction of occurrence-probability of contact for grasp after lift (left), supinate after grasp (middle), and lick after grasp (right) upon closed-loop inhibition of MOs-c IT^{PlxnD1}, PT^{Fezf2} and CT^{Tle4} neurons. Two-sample Kolmogorov-Smirnov test.

D) Impairment of waterspout grasps after lift in prolonged inhibition trials of different PN types. Trials are pooled from 6 IT^{Cux1} mice; 6 IT^{PlxnD1} mice; 7 PT^{Fezf2} mice; 7 CT^{Tle4} mice.

E) Prolonged MOs-c inhibition in IT^{PlxnD1}, PT^{Fezf2}, and CT^{Tle4} increased the probability of premature lick. Wilcoxon rank sum test.

Figure S1

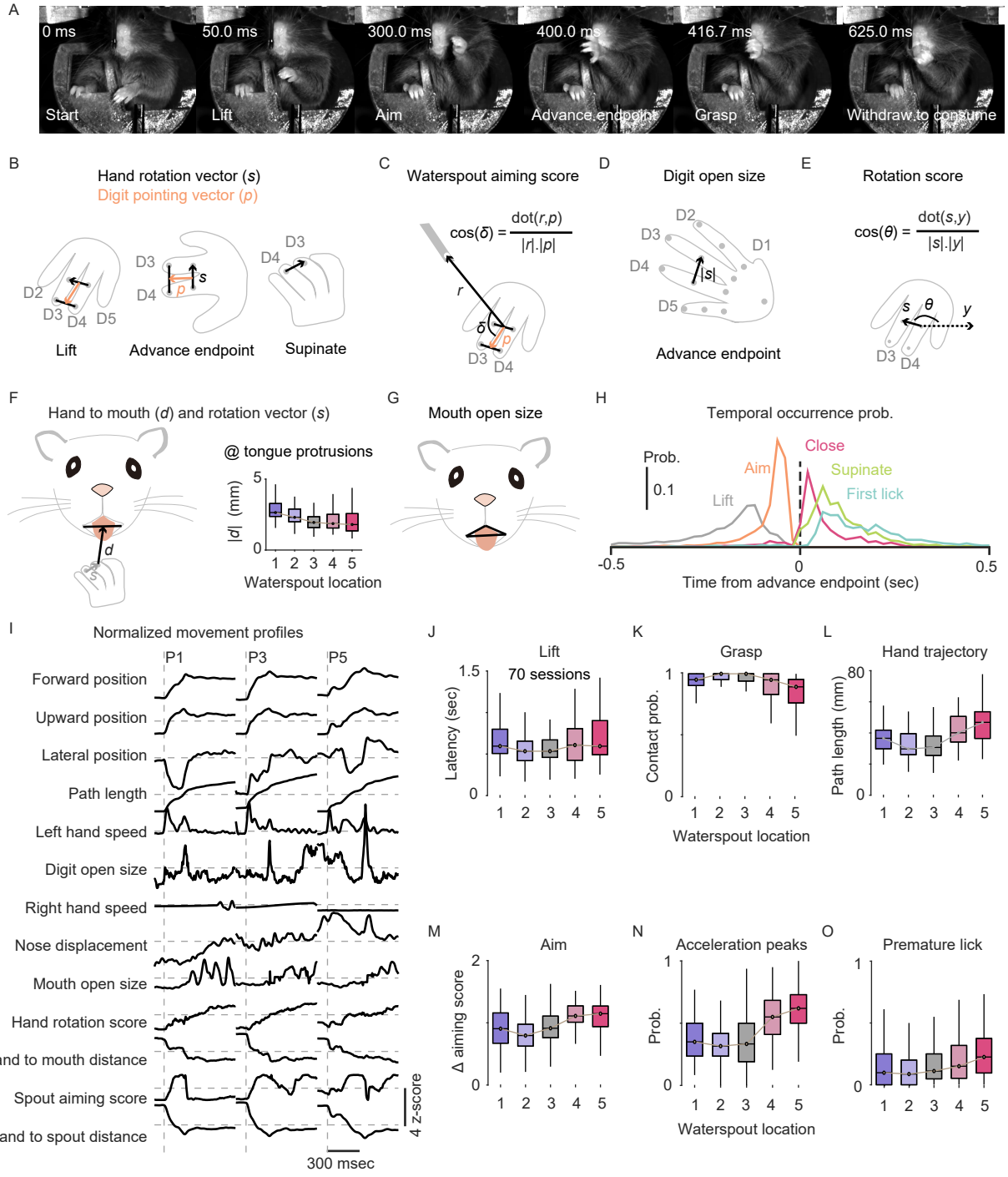

Figure S2

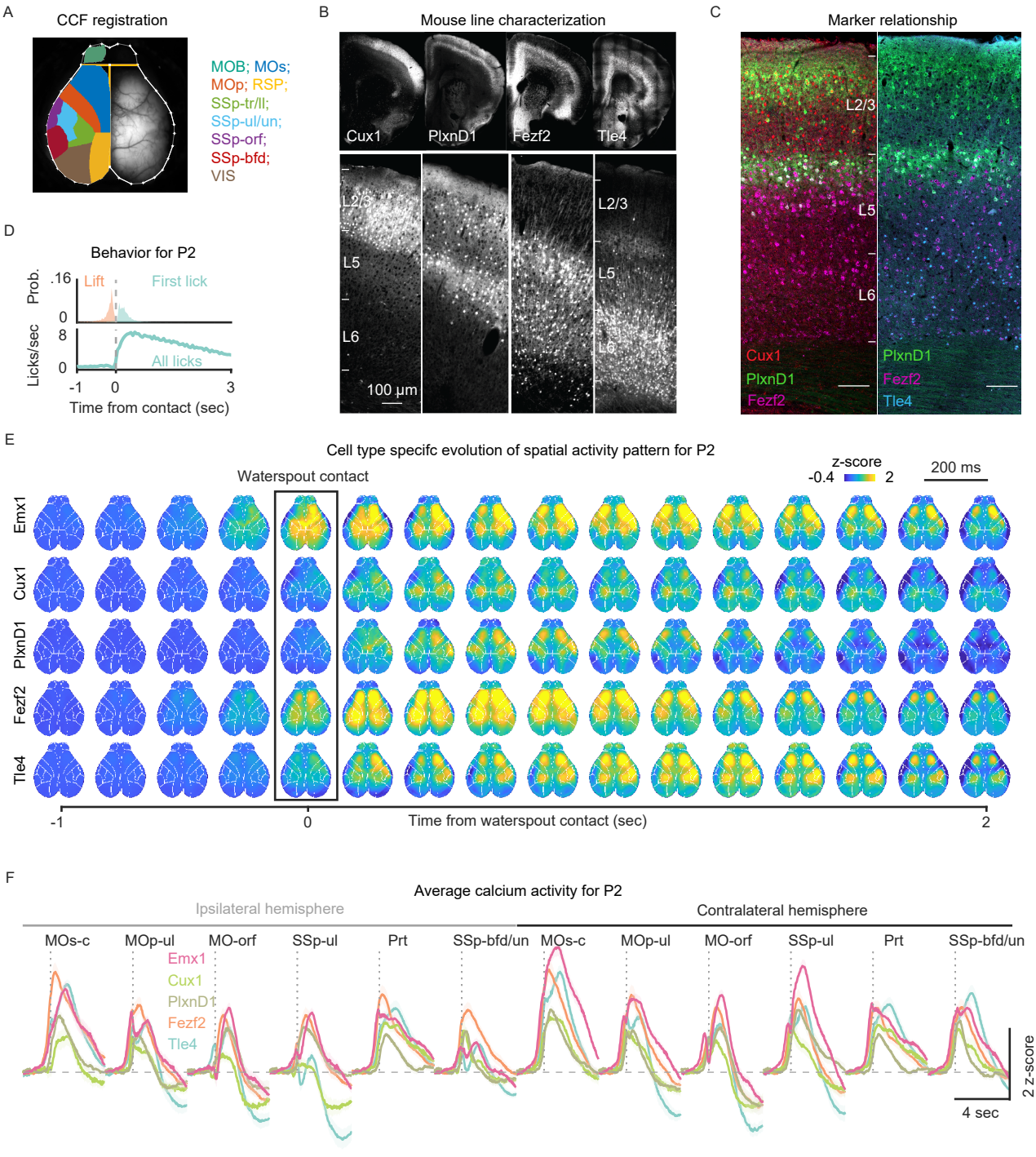

Figure S3

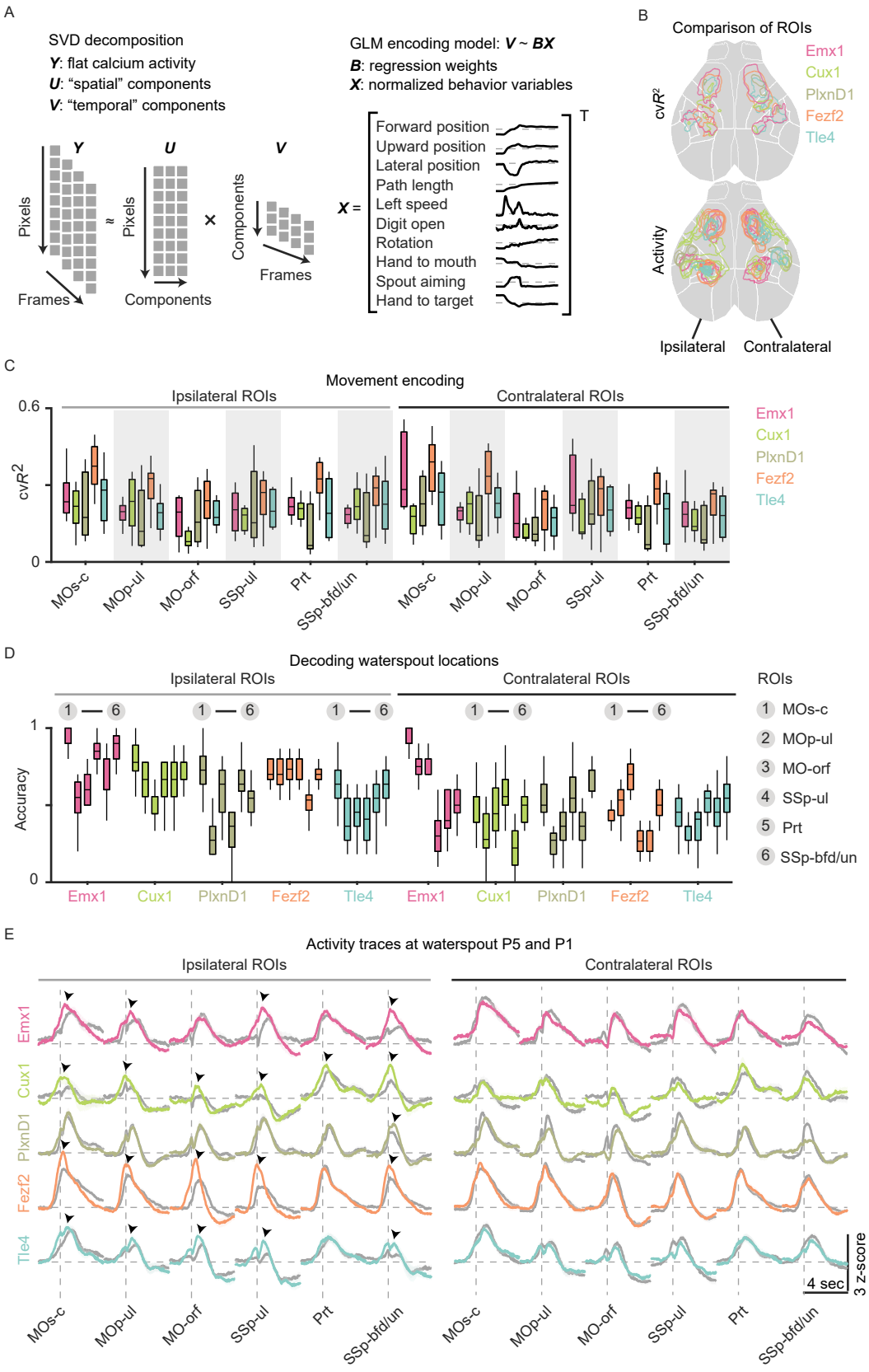

Figure S4

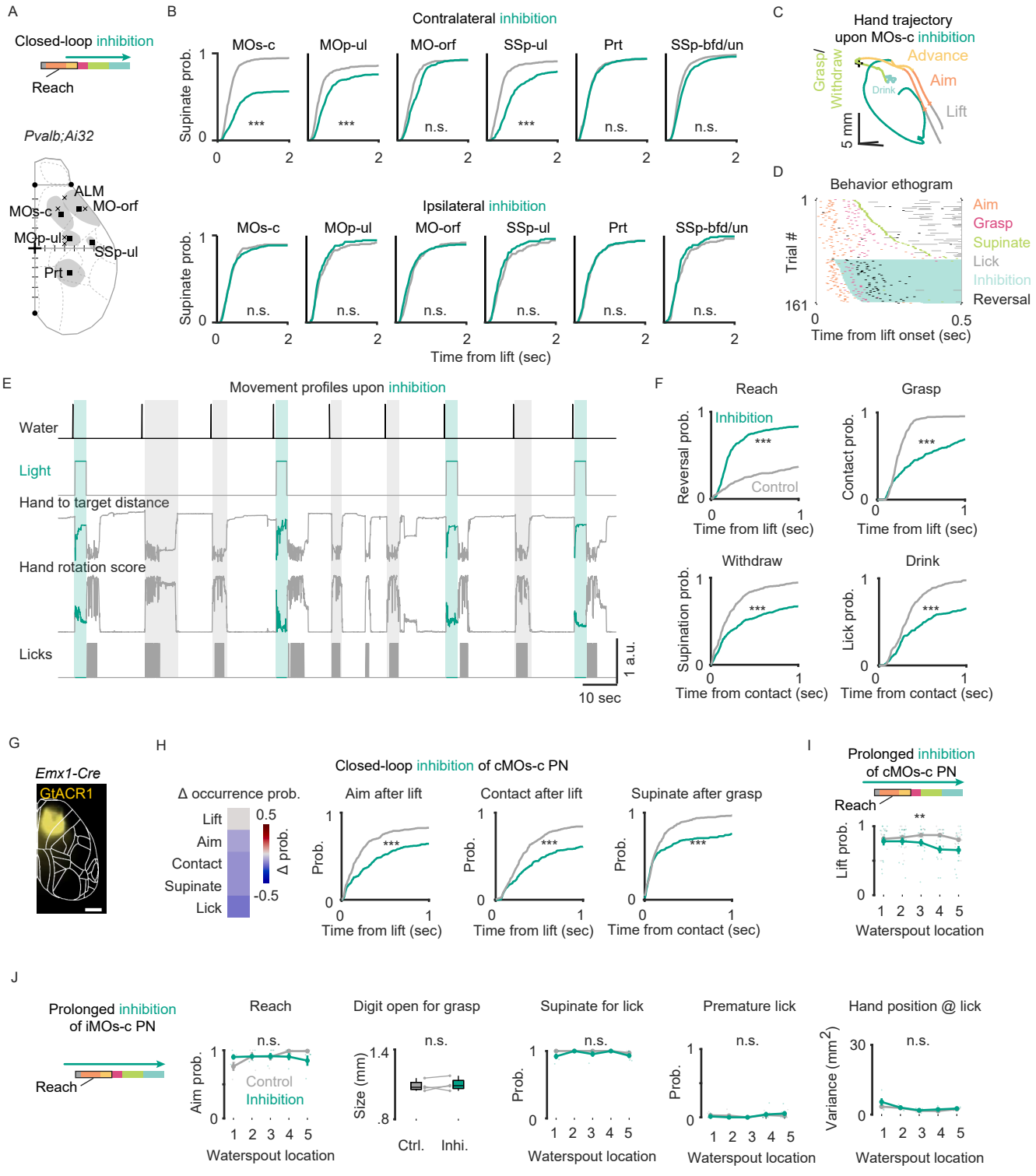

Figure S5

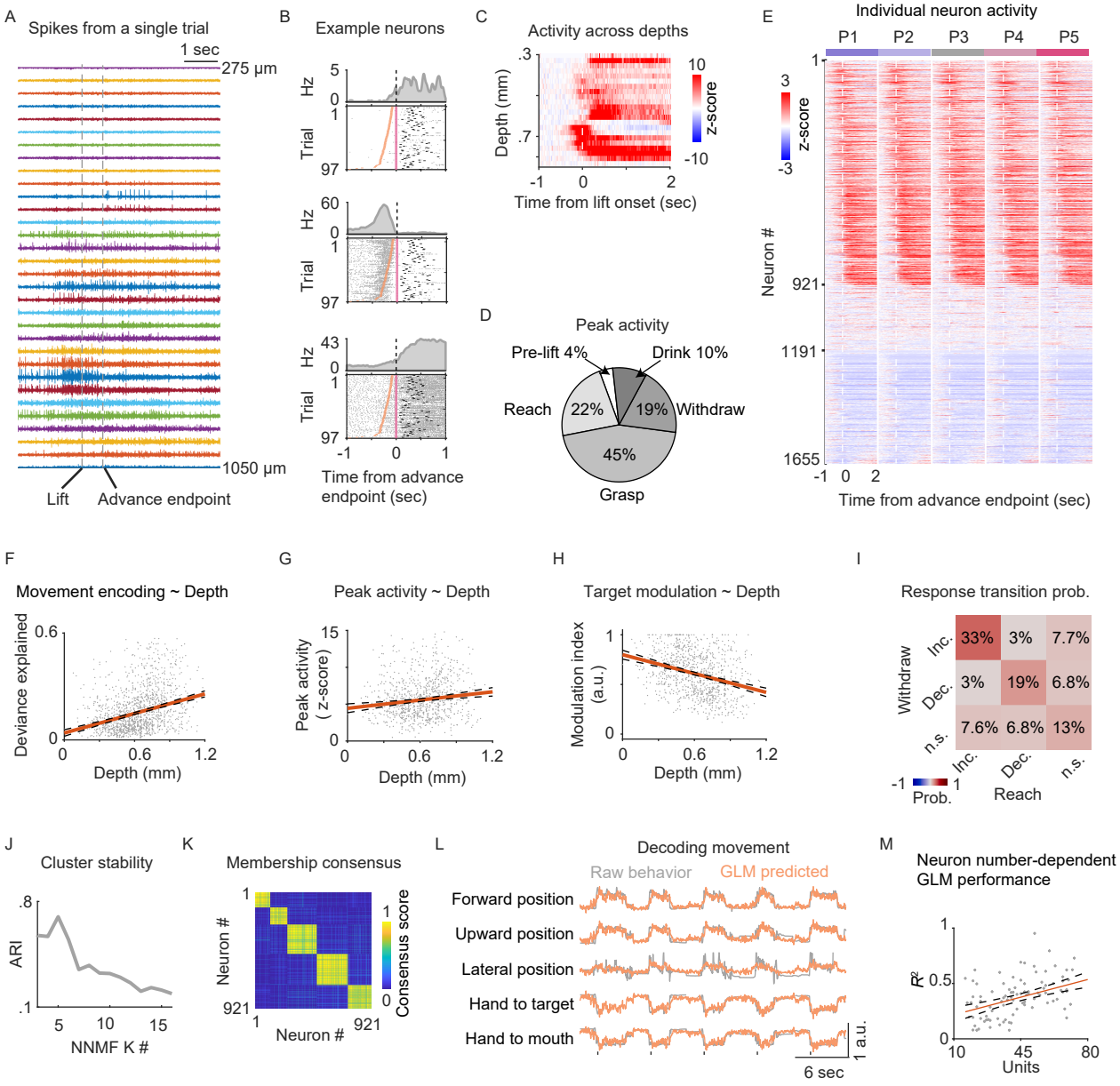

Figure S6

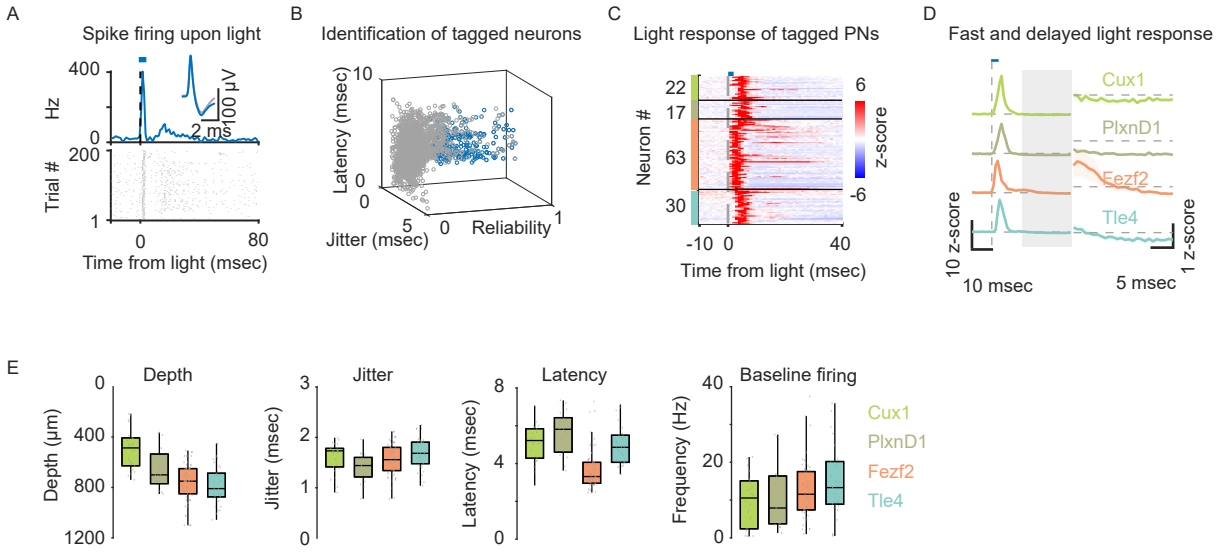

Figure S7

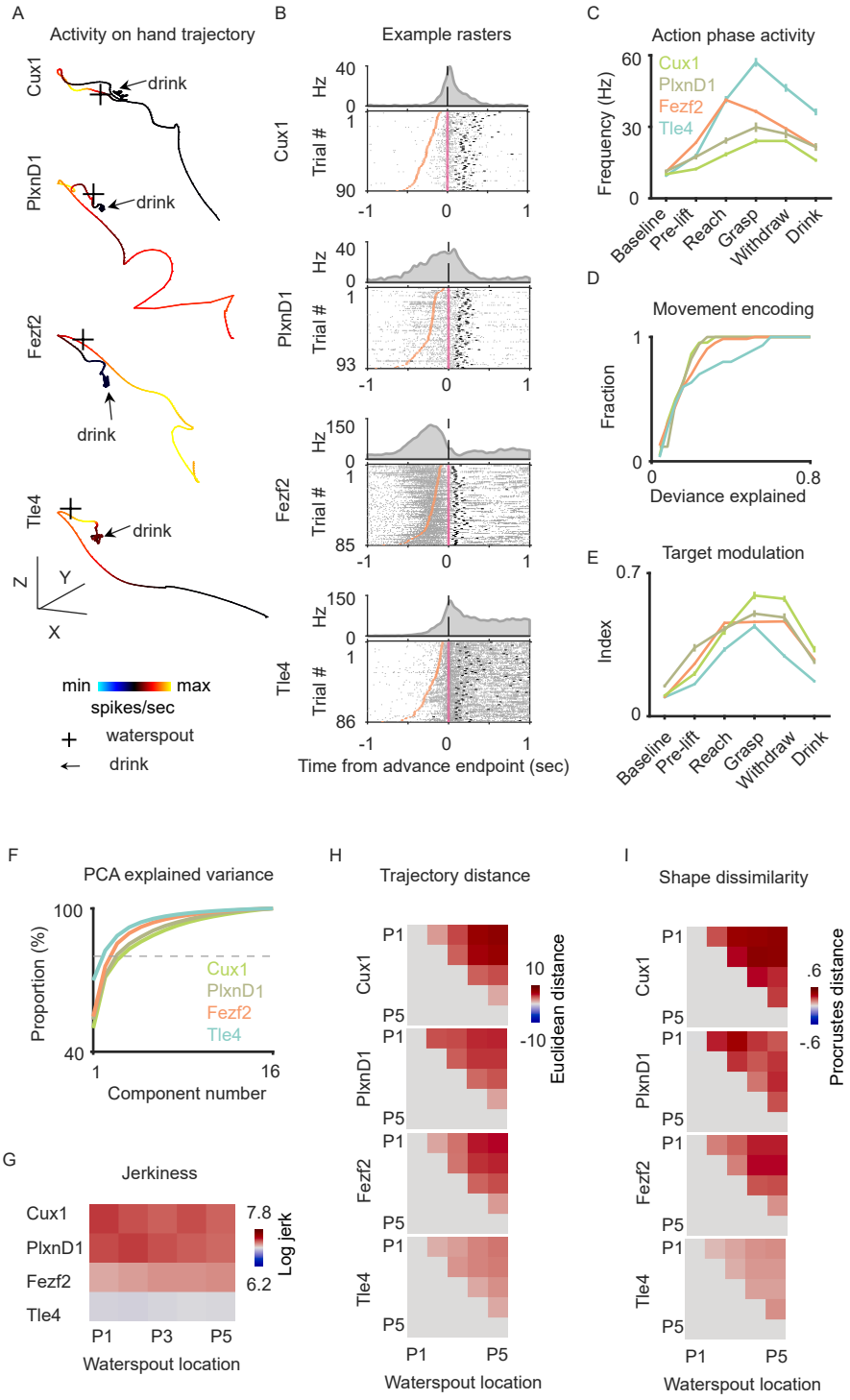

Figure S8